10-21-2017

Spectroscopic and Computational Studies of Reversible O_2 Binding by a Cobalt Complex of Relevance to Cysteine Dioxygenase

Anne A. Fischer
Marquette University

Sergey V. Lindeman
Marquette University, sergey.lindeman@marquette.edu

Adam T. Fiedler
Marquette University, adam.fiedler@marquette.edu

Accepted version. *Dalton Transactions*, No. 39, (June 27, 2017). DOI.

Spectroscopic and Computational Studies of Reversible O_2 Binding by a Cobalt Complex of Relevance to Cysteine Dioxygenase

Anne A. Fischer
Department of Chemistry, Marquette University, Milwaukee, WI
Sergey V. Lindeman
Department of Chemistry, Marquette University, Milwaukee, WI
Adam T. Fiedler
Department of Chemistry, Marquette University, Milwaukee, WI

Abstract

The substitution of non-native metal ions into metalloenzyme active sites is a common strategy for gaining insights into enzymatic structure and function. For some nonheme iron dioxygenases, replacement of the Fe(II) center with a redox-active, divalent transition metal (*e.g.*, Mn, Co, Ni, Cu) gives rise to an enzyme with equal or greater activity than the wild-type enzyme. In this manuscript, we apply this metal-substitution approach to synthetic models of the enzyme cysteine dioxygenase (CDO). CDO is a nonheme iron dioxygenase that initiates the catabolism of L-cysteine by converting this amino acid to the

corresponding sulfinic acid. Two mononuclear Co(II) complexes (**3** and **4**) have been prepared with the general formula $[Co^{2+}(Tp^{R2})(CysOEt)]$ (R = Ph (**3**) or Me (**4**); Tp^{R2} = hydrotris(pyrazol-1-yl)borate substituted with R-groups at the 3- and 5-positions, and CysOEt is the anion of L-cysteine ethyl ester). These Co(II) complexes mimic the active-site structure of substrate-bound CDO and are analogous to functional iron-based CDO models previously reported in the literature. Characterization with X-ray crystallography and/or ^{1}H NMR spectroscopy revealed that **3** and **4** possess five-coordinate structures featuring facially-coordinating Tp^{R2} and *S,N*-bidentate CysOEt ligands. The electronic properties of these high-spin ($S = 3/2$) complexes were interrogated with UV-visible absorption and X-band electron paramagnetic resonance (EPR) spectroscopies. The air-stable nature of complex **3** replicates the inactivity of cobalt-substituted CDO. In contrast, complex **4** reversibly binds O_2 at reduced temperatures to yield an orange chromophore (**4-O$_2$**). Spectroscopic (EPR, resonance Raman) and computational (density functional theory, DFT) analyses indicate that **4-O$_2$** is a $S = 1/2$ species featuring a low-spin Co(III) center bound to an end-on (η^1) superoxo ligand. DFT calculations were used to evaluate the energetics of key steps in the reaction mechanism. Collectively, these results have elucidated the role of electronic factors (*e.g.*, spin-state, d-electron count, metal–ligand covalency) in facilitating O_2 activation and *S*-dioxygenation in CDO and related models.

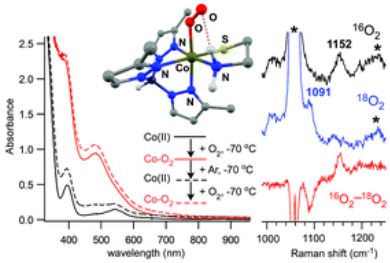

Introduction

Mononuclear nonheme iron dioxygenases (MNIDs) play critical roles in amino acid metabolism,[1–7] the synthesis of complex natural products,[8,9] and the bioremediation of organic pollutants by soil bacteria.[10–15] The active sites of most O_2-activating MNIDs feature an Fe(ii) center bound to the "2-histidine-1-carboxylate facial triad" of protein residues;[16–18]however, in a handful of cases, the carboxylate donor (Asp or Glu) is replaced by a third His ligand.[19–21] The first MNID to exhibit this "3His facial triad" motif in a crystal structure was cysteine dioxygenase (CDO), which initiates the catabolism of l-cysteine (Cys) by catalyzing its conversion to the corresponding sulfinic acid (Scheme 1).[22,23] CDO is essential for regulating the cellular concentration of exogenous Cys, and diminished levels of CDO activity may contribute to the development of neurological disorders in humans.[24–27] Recent studies have demonstrated that the expression of CDO suppresses the growth of tumors, and downregulation of the CDO gene was observed in cancer cell lines.[28] Unlike other MNIDs that are active with non-native metal ions (*e.g.*, Co or Mn),[29] CDO functions exclusively with iron; indeed, addition of Co(ii) salts inhibits CDO by displacing the Fe(ii) center from the active site.[30]

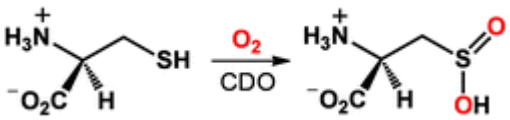

Scheme 1 Reaction catalyzed by CDO.

Experimental and computational studies have contributed to the proposed CDO mechanism shown in Scheme 2, although questions regarding the nature of key intermediates remain. Crystal structures of mammalian CDO have revealed that Cys coordinates directly to the Fe(ii) center in a bidentate manner *via* its thiolate and amine donors, while the carboxylate moiety is stabilized through hydrogen bonds to a second-sphere Arg residue.[31–33] Using nitric oxide (NO) as a mechanistic probe, it was

established that the enzyme follows an ordered mechanism in which Cys coordination precedes the binding of NO (and, presumably, O_2).[34] The spin state and electronic structure of the resulting Fe/O_2 adduct (**A**; Scheme 2) are currently matters of debate.[35,36] It has been proposed that O_2 coordination triggers partial oxidation of the thiolate substrate (**A′**), but the degree of thiyl radical character is uncertain. Unpaired spin density on the S-atom is expected to facilitate formation of a short-lived Fe–O–O–S intermediate (**B**). In the following step, the O–O bond is cleaved to yield an oxoiron(iv) species (**C**) bound to a –S(O)R ligand.[36–40] Subsequent O-atom transfer to the sulfenate ligand generates the dioxygenated product bound to an Fe(ii) center (**D**).

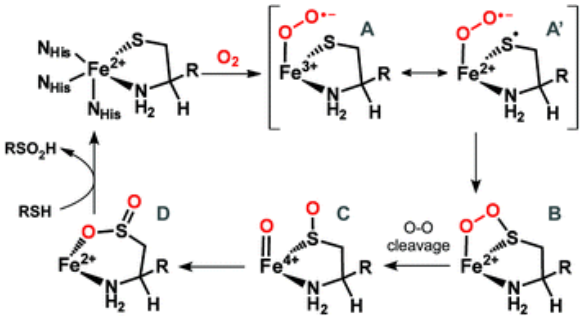

Scheme 2 Proposed catalytic cycle of CDO.

Our understanding of CDO catalysis has been advanced through the development of synthetic models that replicate key features of the enzyme active site.[41–48] In 2012, the Limberg group reported the five-coordinate complex [Fe($Tp^{Ph,Me}$)(CysOEt)] (**1**), where $Tp^{Ph,Me}$ is hydrotris(3-phenyl-5-methylpyrazolyl)borate and CysOEt is the anion of l-cysteine ethyl ester (Scheme 3).[46] More recently, our group employed the tris(4,5-diphenylimidazol-2-yl)phosphine chelate (2-TIP^{Ph2}; Scheme 3) to generate the related CDO mimic [Fe(2-TIP^{Ph2})(CysOEt)]BPh_4 (**2**).[49] The 2-TIP^{Ph2} and $Tp^{Ph,Me}$ supporting ligands both replicate the facial N3 coordination of the 3His triad, but the former matches the neutral charge of the enzymatic environment. Complexes **1**and **2** are pale yellow due to the presence of overlapping S → Fe(ii) charge transfer (CT) transitions in the near UV region, which we deconvoluted with the aid of MCD spectroscopy. These CT bands decay slowly upon treatment of **1** or **2** with excess O_2 at room temperature following pseudo first-order kinetics. Interestingly, our studies found that the rate of reaction is nearly independent of supporting ligand ($Tp^{Ph,Me}$ or 2-TIP^{Ph2}). The observed spectral changes are indicative of sulfur oxidation, and the sulfinic acid products were detected by ^{1}H NMR spectroscopy. Therefore, complexes **1** and **2** serve as structural and functional models of CDO.

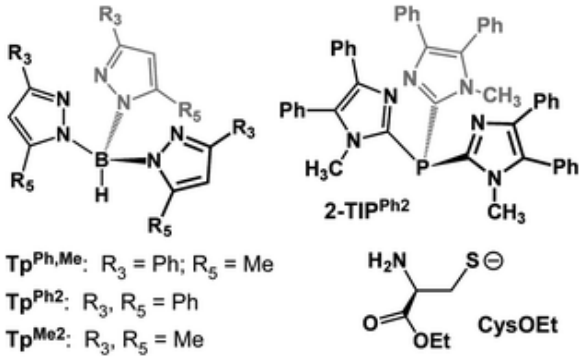

Scheme 3 Ligands employed in CDO modeling studies.

Because high-spin Fe(ii) centers in nonheme environments lack intense absorption features in the visible region and possess integer ($S = 2$) spin ground states, it is not possible to directly examine **1** and **2** with resonance Raman (rRaman) or electron paramagnetic resonance (EPR) spectroscopies. In our previous report, this limitation was overcome by treating the CDO models with the O_2-surrogate NO, which generated a mixture of EPR-active Fe/NO adducts possessing $S = 3/2$ or $1/2$ ground states.[49] Another well-

established strategy for probing the geometric and electronic structures of nonheme iron enzymes (and related model complexes) involves replacement of the Fe(ii) center with a divalent metal ion that is more spectroscopically "accessible", such as Co(ii), Mn(ii), or Cu(ii).[50–53] In addition to enhancing the spectroscopic features of the enzymes, metal-substitution experiments often yield valuable insights into O_2activation mechanisms, as recently demonstrated by Que and Lipscomb in their studies of Co(ii)- and Mn(ii)-substituted versions of homoprotocatechuate-2,3-dioxygenase, a MNID that catalyzes the oxidative ring-cleavage of its catechol substrate.[54–58]

This manuscript describes the synthesis, characterization, and O_2 reactivity of Co(ii)-containing models of the CDO active site with the general formula [Co(Tp^{R2})(CysOEt)], where R = Ph (**3**) or Me (**4**). Our motivation for pursuing these Co-containing mimics is three-fold. Firstly, as demonstrated below, comparative studies of Fe and Co complexes **1–4** highlight the impact of redox potential, spin-state, d-electron count, and steric properties on O_2 reactivity, and these findings have significant implications for the enzymatic mechanism. Secondly, complexes **3** and **4**, as well as intermediates derived from their reaction with O_2, possess half-integer spin states and an abundance of absorption features in the visible region, thus permitting analysis with multiple spectroscopic techniques (EPR, UV-vis absorption, rRaman, paramagnetic NMR) that provide complementary electronic-structure information. Finally, the cobalt-based approach has allowed us to isolate and spectroscopically characterize a dioxygen-bound adduct (**4-O_2**), which is significant given that iron congeners of this species have eluded detection in both CDO and related model complexes. Furthermore, cobalt(iii)-superoxo intermediates like **4-O_2**are likely involved in numerous catalytic processes, including the aerobic oxidation of organic compounds[59,60] and oxygen-reduction reactions.[61–63] To gain a better understanding of the spectroscopic and chemical features of the Co- and Fe-CDO models, density functional theory (DFT) calculations were utilized to generate molecular bonding descriptions, computed spectroscopic parameters, and potential energies surfaces of putative O_2 activation mechanisms. Collectively, these results furnish a convincing answer to the question of why CDO, unlike some other MNIDs, lacks activity with cobalt, while simultaneously illuminating the essential role played by iron in the native enzyme.

Results and discussion

Co(ii)-Based CDO models

Synthesis, X-ray crystallography, and solution structures from NMR data

Complexes **3** and **4**were prepared by reaction of [Co(Tp^{Ph2})(OAc)(Hpz^{Ph2})] (Hpz^{Ph2} = 3,5-diphenylpyrazole) or [Co(Tp^{Me2})(OAc)] (**5**) precursors, respectively, with a slight excess of l-cysteine ethyl ester hydrochloride (H-CysOEt·HCl) in CH_2Cl_2. The reactions employed two equivalents of triethylamine as the base, followed by work up to eliminate byproducts. The resulting maroon (**3**) or dark purple (**4**) complexes exhibit effective magnetic moments (μ_{eff}) of ~4.8μ_B in $CDCl_3$, typical of mononuclear, high-spin ($S = 3/2$) Co(ii) complexes.[64,65] Observation of an intense ν(CO) peak at 1729 cm^{-1} in the IR spectra of both complexes confirms coordination of the CysOEt ligand (by comparison, the highest-energy ν(CO) mode of the acetate precursors appears near ~1550 cm^{-1}).[66]

Dark brown crystals of **3** suitable for crystallographic analysis were obtained by layering CH_2Cl_2 solutions with MeCN; details concerning the X-ray diffraction experiments are provided in the Experimental section. Complex **3** crystallizes in the chiral space group $P2_1$ due to the presence of the chiral CysOEt ligand. Each unit cell consists of two symmetrically-independent five-coordinate (5C) Co(ii) complexes featuring different conformations of the 3-Ph substituents of the Tp^{Ph2} ligand. Metric parameters for both independent molecules are provided in Table 1, in addition to previously-reported values for the iron analogue **1**. The X-ray structure of **3**, shown in Fig. 1, reveals that the monoanionic CysOEt ligand binds to Co(ii) in a *S,N*-bidentate manner and the Tp^{Ph2} chelate exhibits facial κ^3-coordination, thus reproducing the active-site structure of substrate-bound CDO. The coordination geometry of **3** is best described as trigonal

bipyramidal, as reflected in the average tau-value of 0.60.[67,68] The Co–N_{Tp} bond distances, ranging between 2.08 and 2.20 Å, are characteristic of high-spin Co(ii) complexes and similar to those exhibited by complex **1** (Table 1). The Co–S1 and Co–N7 distances involving the CysOEt ligand, however, are shorter than their counterparts in **1** by 0.055 and 0.085 Å, respectively, perhaps due to the smaller ionic radius of Co(ii) compared to Fe(ii).

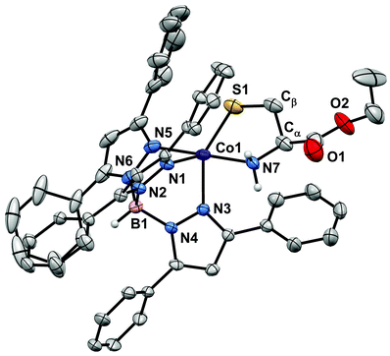

Fig. 1 Thermal ellipsoid plot (50% probability) derived from the X-ray crystal structure of **3**. Most hydrogen atoms have been omitted for clarity.

Table 1 Selected bond distances (Å) and bond angles (°) for complexes **1** and **3** as determined by X-ray diffraction (XRD) and DFT calculations

	1 (M = Fe)[a]	3 (M = Co)[b]		3 (M = Co)
Method	**XRD**	**XRD (A)**	**XRD (B)**	**DFT**
Bond distances				
M1–N1	2.106(2)	2.088(3)	2.100(3)	2.159
M1–N3	2.112(2)	2.095(3)	2.080(3)	2.079
M1–N5	2.275(2)	2.179(3)	2.198(3)	2.137
M1–S1	2.3122(9)	2.256(1)	2.258(1)	2.272
M1–N7	2.290(3)	2.201(3)	2.208(3)	2.237
Bond angles				
N1–Fe1–N3	95.36(9)	93.9(1)	94.2(1)	93.0
N1–Fe1–N5	82.29(9)	82.8(1)	82.9(1)	85.4
N1–Fe1–S1	134.21(7)	142.97(9)	137.18(9)	141.8
N1–Fe1–N7	89.30(9)	92.4(1)	94.6(1)	87.0
N3–Fe1–N5	85.29(9)	88.9(1)	88.5(1)	86.6
N3–Fe1–S1	130.07(7)	123.10(9)	128.65(9)	124.4
N3–Fe1–N7	92.04(9)	93.3(1)	92.3(1)	91.9
N5–Fe1–S1	104.07(6)	97.02(8)	96.39(9)	102.9
N5–Fe1–N7	170.88(9)	174.8(1)	177.5(1)	172.2
S1–Fe1–N7	84.32(7)	85.75(9)	85.02(9)	84.3
τ-Value	0.61	0.53	0.67	0.51

a Parameters obtained from ref. 46. b The unit cell of complex 3 contains two symmetry-independent Co(ii) molecules, labeled A and B in the table.

Our repeated efforts to grow X-ray quality crystals of **4** were not successful. However, we are confident that complexes **3** and **4** share the same general [Co(Tp^{R2})(CysOEt)] structure based on similarities between their spectroscopic profiles. The UV-vis absorption and EPR features of both complexes are discussed in the following sections. Here, we focus first on ^{1}H NMR spectra of **3–5** measured at room temperature in $CDCl_3$ solutions. The spectrum of [Co(Tp^{Me2})(OAc)] (**5**) provides a helpful starting point. As shown in Fig. 2,

complex **5** exhibits peaks arising from the 3-Me and 5-Me pyrazole substituents at −41 and 35 ppm, respectively, while the 4-pyrazole protons appear at 62 ppm. These chemical shifts are consistent with previously-reported spectra of Tp-based Co(ii) complexes.[69,70] The spectrum of **4** is more complex; in addition to the four Tp^{Me2}-derived features, it displays a series of peaks arising from the CysOEt ligand (marked with the black dots in Fig. 2). Based on integrations, the resonances at −5.3, −6.6, and −48 ppm (1H each) are assigned to the three protons attached to the C_α and C_β atoms of CysOEt. The peaks at −4.1 (3H) and 1.3 (2H) ppm are then attributed to the –CH_3 and –OCH_2– units, respectively, of the ethoxide moiety. The same pattern of CysOEt-derived peaks is observed in the spectrum of **3** with only minor deviations in δ-values (Fig. 2; see inset), proving that the coordination geometries of **3** and **4** are equivalent. The Tp^{Ph2}-based features of **3** were assigned through comparisons to spectra reported for related complexes.[71–73] It is notable that, for each complex, the three pyrazole rings are spectroscopically equivalent in solution, suggesting that the positions of the acetate (**5**) or CysOEt (**3** and **4**) ligands are dynamically averaged on the NMR time scale.

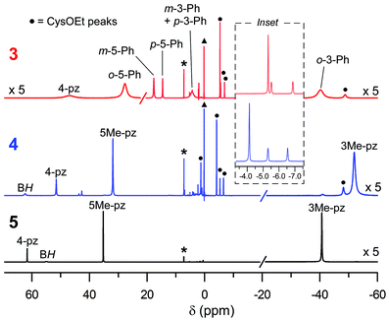

Fig. 2 ^{1}H NMR spectra of complexes **3** (top, red), **4** (middle, blue), and **5** (bottom, black) in $CDCl_3$ at room temperature. Spectra were referenced using residual solvents peaks (indicated by *) and tetramethylsilane (indicated by ▲). Peaks marked with black dots (●) arise from the CysOEt ligand of **3** and **4**. As indicated on the figure, some peak intensities were increased for the sake of clarity.

Electronic properties of [Co(Tp^{R2})(CysOEt)] (R = Me, Ph): absorption spectroscopy and time-dependent DFT

Electronic absorption spectra of complexes **3–5**, measured in CH_2Cl_2 at room temperature, are presented in Fig. 3. All three complexes exhibit a series of features in the 500–1100 nm region (Fig. 3; inset) that arise from Co(ii) ligand field (d–d) transitions, as evidenced by their low intensities ($\varepsilon < 150$ M^{-1} cm^{-1}). Following assignments reported for other trigonal bipyramidal Co(ii) complexes,[74–76] the closely-spaced peaks between 500 and 650 nm are attributed to transitions from the $^4T_{1g}$(F) ground-state in the parent O_h symmetry to components of the$^4T_{1g}$(P) excited state. The weaker bands at ~680 and 900 nm in the spectra of **3** and **4** are then assigned to components of the lower-energy $^4T_{2g}$(F) term that split dramatically in low-symmetry environments.[74,75] The ligand-field (LF) features of **3** and **4** are strikingly similar, providing further confirmation that these two complexes possess nearly identical Co(ii) coordination geometries.

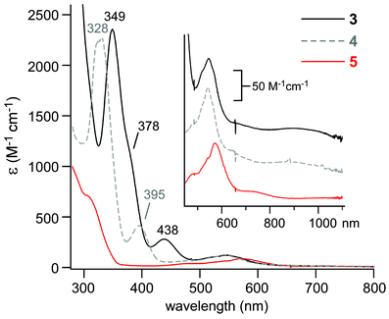

Fig. 3 Electronic absorption spectra of Co(ii) complexes **3–5** measured at room temperature in CH_2Cl_2. Inset: Ligand-field transition observed in the visible region; spectra are offset along the *y*-axis for the sake of clarity.

In addition to the LF features, complexes **3** and **4** exhibit two peaks of greater intensity in the near UV-region (349 and 438 nm for **3**; 328 and 395 nm for **4**; see Fig. 3); a third band appears as a shoulder on the more intense feature. These bands, which are absent in the absorption spectrum of **5**, arise from S → Co(ii) charge transfer (CT) transitions. This assignment is supported by time-dependent DFT calculations (discussed below) and literature precedents.[77–79] The CT bands of **4** are blue-shifted by ~2000 cm^{-1} relative to those observed for **3**, reflecting the ability of the 3,5-pyrazole substituents to modulate the donor strength of the Tp^{R2}scaffold. Our results indicate that changes to the Tp ligand cause the energies of the cobalt d-orbitals to shift uniformly; hence, the LF transition energies – unlike the CT transition energies – are largely unaffected by replacement of Tp^{Me2} with Tp^{Ph2}.

DFT methods provided further insights into the electronic structures of the Co-CDO models. Using a truncated version of the crystallographic structure of **3** as a starting point, geometry optimization yielded a computational model that accurately reproduces the experimental Co–N/S bond angles and distances (Table 1). This model was applied to time-dependent DFT (TD-DFT) studies employing the cam-B3LYP range-separated hybrid functional.[80] In agreement with the experimental data, the TD-DFT computed spectrum (Fig. S1‡) consists of a series of LF bands with $\lambda_{max} > 450$ nm and three S → Co(ii) CT transitions in the 300–400 nm region. The LF and CT transitions primarily involve the Co(ii)- and ligand-based molecular orbitals (MOs) depicted in the energy level diagram shown in Fig. 4. The two spin-down (β) Co electrons are localized in Co(d_{xz})- and Co(d_{yz})-based MOs, consistent with the trigonal–bipyramidal coordination geometries of **3** and **4**. The donor MOs for the CT transitions are two S(3p)-based MOs located on the thiolate donor; the S_π MO is oriented perpendicular to the Co–S bond, while the S_σ MO lies along the Co–S bond vector (Fig. 4). Electron density difference maps indicate that the lowest-energy CT band arises from a S_π → Co($d_{x^2-y^2}$) transition that lacks significant intensity due to poor orbital overlap. In contrast, the more intense CT band in the UV region exhibits S_σ → Co(ii) (σ → σ*) character. Similar assignments were made for the series of S → Fe(ii) CT transitions observed in our previous study of Fe(ii)-based models **1** and **2**.[49]

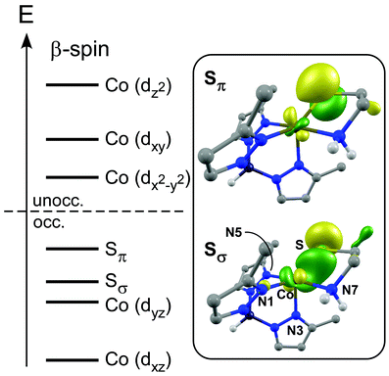

Fig. 4 Energy-level diagram for the spin-down (β) molecular orbitals (MOs) obtained from a spin-unrestricted DFT calculation of a truncated [Co(Tp^{R2})(CysOEt)] model. MOs are labeled according to their principal contributor. Inset: DFT-generated isosurface plots of the CysOEt-based donor MOs involved in S → Co(ii) CT transitions.

Electronic properties of [Co(Tp^{R2})(CysOEt)] (R = Me, Ph): EPR spectroscopy

Low-temperature (7.5 K) X-band EPR spectra of **3** and **4** in frozen CH_2Cl_2 are shown in Fig. 5. Both spectra are quite complex with multiple resonances observed across a wide field range of 200 to >9000 G. As with the ^{1}H NMR and UV-vis data, the EPR spectra of **3** and **4** are similar in most respects. The primary difference is that samples of **4** exhibit a sharp derivative-shaped feature in the $g = 2$ region ($B \sim 3350$ G) due to a

small amount of the dioxygenated complex **4-O$_2$** (*vide supra*); this feature has been truncated in Fig. 5 for the sake of clarity. To rule out the possibility that some of the observed resonances are due to residual amounts of the precursor complexes, EPR spectra of [Co(Tp^{Ph2})(OAc)(Hpz^{Ph2})] and **5** were collected under identical conditions. Based on the resulting spectra, it was verified that cobalt-acetate impurities do not contribute to the EPR spectra of **3** and **4**. The simulated EPR spectra (red lines in Fig. 5) nicely reproduce the key features of the experimental data. The spin-Hamiltonian parameters derived from these simulations (Table 2) are broadly consistent with those reported by Tierney and coworkers for pentacoordinate Co(ii) complexes with Tp ligands.[81]

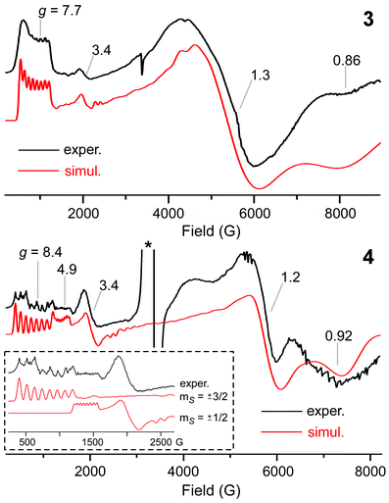

Fig. 5 X-band EPR spectra of complexes **3** (top) and **4** (bottom) measured in frozen CH_2Cl_2 at 7.5 K. Parameters: frequency = 9.625 GHz; power = 2.0 mW; modulation amplitude = 1.0 G. The corresponding simulations (red lines) assumed a $S = 3/2$ ground state and utilized the spin-Hamiltonian parameters provided in Table 2. Inset: Expansion of the low-field region. Simulated contributions from the $m_S = \pm 1/2$ and $\pm 3/2$ doublets are shown in red.

Table 2 EPR simulation parameters for complexes **3** and **4**

Complex	g_x	g_y	g_z	D (cm^{-1})	E/D	^{59}Co A_z (G)
3	2.68	2.58	2.03	−14	0.15	96
4	2.92	2.25	2.05	−9	0.17	106

The EPR spectra of **3** and **4** are dominated by features arising from the $m_S = \pm 3/2$ doublet of the $S = 3/2$ manifold, indicative of a negative axial zero-field-splitting (zfs) term (*i.e.*, $D < 0$). The $m_S = \pm 3/2$ doublet is responsible for the broad band at high field ($g \sim 0.9$), the derivative signal centered at $g = 1.3$, and the low-field peak near $g = 8$. The latter displays hyperfine splitting from the ^{59}Co nucleus ($I = 7/2$), in addition to poorly-resolved superhyperfine structure from a single nitrogen atom (Fig. 5; inset). Signals from the higher-energy $m_S = \pm 1/2$ doublet are also evident in both spectra, namely, the derivative-shaped feature at $g = 3.4$ and the broad band at $g = 4.9$. The simulated spectra in the inset of Fig. 5 depict the respective contributions of the $m_S = \pm 1/2$ and $\pm 3/2$ doublets to the low-field features in the spectrum of **4**. The diminished intensity of the $m_S = \pm 1/2$ resonances in the spectrum of **3** reflects the more negative D-value (−14 cm^{-1}) of this complex compared to **4** (−9 cm^{-1}; Table 2). Both species exhibit moderate rhombicity with E/D-values near 0.16 (E is the rhombic zfs term), suggesting that the distorted N_4S coordination environment observed in the solid-state is maintained in solution. For reasons that are not clear to us, there are modest differences between the **g**-tensors of **3** and **4** (Table 2); regardless, both sets of g-values are comparable to those previously-reported for related Co(ii) complexes.[69,81]

Electrochemical studies of [Co(Tp^{R2})(CysOEt)] (R = Me, Ph)

The redox properties of **3** and **4**were measured in CH_2Cl_2 solutions with 0.1 M $[NBu_4]PF_6$ as the supporting electrolyte. The resulting cyclic voltammograms (CV), shown in Fig. 6, were referenced to the ferrocenium/ferrocene couple (Fc^+/Fc). Both complexes exhibit a single redox event that corresponds to one-electron oxidation of the Co(ii) center. The redox couple observed for **3** is quasi-reversible ($\Delta E = 135$ mV) whereas **4** displays greater splitting between cathodic and anodic peaks ($\Delta E = 370$ mV). Comparison of redox potentials ($E_{1/2} = +0.01$ and -0.23 for **3** and**4**, respectively) indicates that the Co(iii/ii) potential is sensitive to the identity of the pyrazole substituents, as replacement of Tp^{Me2} with Tp^{Ph2} causes a shift of +240 mV. These results are consistent with the trend in S → Co(ii) CT energies noted above. The ability of the Tp^{Me2} ligand to depress the Co(ii/iii) potential likely enhances the reactivity of **4** towards O_2, as described in the next section.

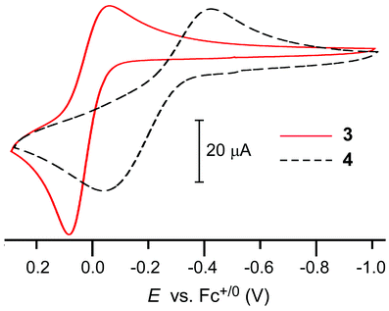

Fig. 6 Cyclic voltammograms of **3** and **4**. Data was collected in CH_2Cl_2 with 0.1 M $[NBu_4]PF_6$ as the supporting electrolyte and a scan rate of 200 mV s^{-1}. Sample concentrations were 2.7 and 2.4 mM for **3** and **4**, respectively.

Dioxygen reactivity of complexes 3 and 4

Formation of a cobalt-dioxygen adduct (4-O_2) – spectroscopic and computational studies

The absorption features of **3** in CH_2Cl_2 remain unchanged after several days of exposure to O_2at room temperature. The stability of **3** in air is not due to steric factors, as its iron congener (**1**) reacts with O_2 to yield the sulfinic acid derivative of CysOEt.[46] Moreover, our previous spectroscopic studies demonstrated that both **1** and **2** are able to bind nitric oxide (NO), proving that Tp^{Ph,Me} and 2-TIP^{Ph2} supporting ligands cannot prevent O_2 from accessing the M(ii) center.[49] Although complex **3** features a Tp^{Ph2} ligand instead of Tp^{Ph,Me}, the identity of the 5-substituent is not expected to impact small molecule binding due to its distance from the metal ion. Thus, the side-by-side comparison of complexes **1** and **3** suggests that Co(ii) is *intrinsically* less capable than Fe(ii) of activating O_2 for *S*-dioxygenation in this particular ligand environment.

Whereas **3** is unreactive towards O_2 under all conditions tested, treatment of complex **4** with O_2 at low temperatures generates an orange intermediate (**4-O_2**) with absorption bands at 385 and 483 nm (Fig. 7). Formation of **4-O_2** is apparent at temperatures as high as −20 °C, but complete conversion requires temperatures below −70 °C. Bubbling argon through cooled solutions of **4-O_2**, or warming the sample to room temperature, causes the original Co(ii) spectrum to fully reappear, indicative of reversible O_2 binding. The inset of Fig. 7 highlights the reversibility of this process by depicting the formation and disappearance of the **4-O_2**chromophore during three successive cycles of O_2 and Ar purges.

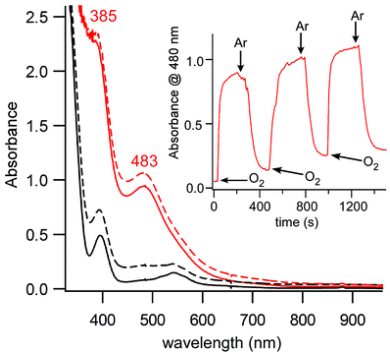

Fig. 7 UV-visible spectral changes during the reaction of complex **4** with O_2 at −70 °C in CH_2Cl_2. Treatment of the starting complex (black solid line) with O_2 yields **4-O₂** (red solid line). Purging with Ar regenerates **4** (black dashed line) and subsequent exposure to O_2 returns the spectrum of **4-O₂** (red dashed line). Inset: Time traces of absorption intensity at 480 nm during successive purges of CH_2Cl_2 solutions of **4**with O_2 and Ar at −70 °C.

The geometric and electronic structures of **4-O₂** were probed with spectroscopic methods. The X-band EPR spectrum of **4-O₂**, measured in frozen CH_2Cl_2 at 60 K, exhibits a quasi-axial $S = 1/2$ signal with g-values of 2.10, 2.02, and 1.98 (Fig. 8). The hyperfine splitting from the ^{59}Co nucleus is clearly evident in the g_z-region of the second-harmonic spectrum, whereas hyperfine splitting within the g_y-component is less clearly resolved. The small magnitude of the ^{59}Co hyperfine splitting ($A_z = 22$ G; compared to 106 G for **4**) indicates that the unpaired electron is not localized on the cobalt center. Instead, the EPR features resemble those previously-reported for mononuclear, low-spin cobalt(iii)-superoxide species.[57,64,82–85] This conclusion is confirmed by rRaman measurements that provide definitive proof of Co/O_2adduct formation. Spectra of **4-O₂** collected with 501.7 nm laser excitation (Fig. 9) revealed a ν(O–O) mode at 1152 cm^{-1} that shifts to 1091 cm^{-1} upon $^{18}O_2$ substitution ($\Delta^{18}O = 61$ cm^{-1}). Such frequencies are characteristic of superoxo ligands bound to transition-metals in an end-on (η^1) manner.[64,85–89]

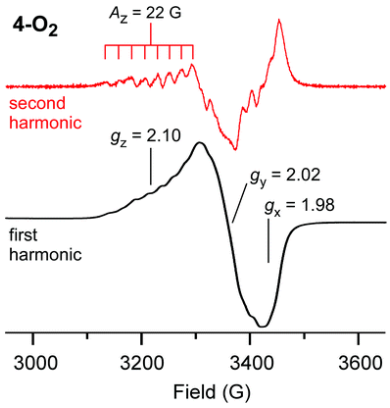

Fig. 8 X-band EPR spectrum of **4-O₂** in frozen CH_2Cl_2 at 60 K. The second harmonic spectrum (red line) highlights the ^{59}Co hyperfine splitting. Parameters: frequency = 9.48 GHz; power = 1.0 mW; modulation amplitude = 10 G.

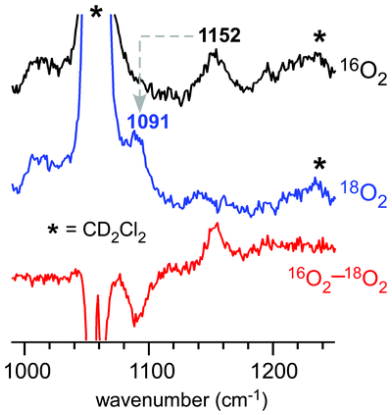

Fig. 9 Resonance Raman spectra (λ_{ex} = 501.7 nm, 10 mW, 77 K) of **4-O₂** in frozen CD_2Cl_2 prepared with $^{16}O_2$ (top, black line) and $^{18}O_2$ (middle, blue line). The $^{16}O_2$–$^{18}O_2$ difference spectrum (bottom, red line) reveals the presence of isotopically-active peaks. Peaks arising from CD_2Cl_2 are indicated with the asterisk.

The DFT-derived structure of **4-O₂**, shown in Fig. 10(a), consists of a six-coordinate cobalt center coordinated to an O_2 ligand in a bent conformation (Co–O–O angle of 121°). The computed O–O distance of 1.296 Å and ν(O–O) frequency of 1204 cm^{-1} are consistent with the superoxo nature of the O_2 ligand. The negative charge of the $O_2^{\bullet-}$ moiety facilitates formation of a hydrogen bond between the distal atom (O2) and the –NH_2 donor of CysOEt. As illustrated in Fig. 10(b), the Co(iii) center of **4-O₂** is low-spin with a $[d_{xz}^2, d_{yz}^2, d_{xy}^2, d_{x^2-y^2}^0. d_{z^2}^0]$ configuration, which is also apparent in the shortening of the Co–N_{Tp} bonds relative to the high-spin Co(ii) precursor. The unpaired electron is almost entirely localized in the O_2 π_{op}*-based MO, where "op" indicates that the orbital lies out of the Co–O–O plane. The corresponding in-plane π_{ip}* MO is doubly-occupied and participates in a σ-bonding interaction with the Co(d_{z^2}) orbital.

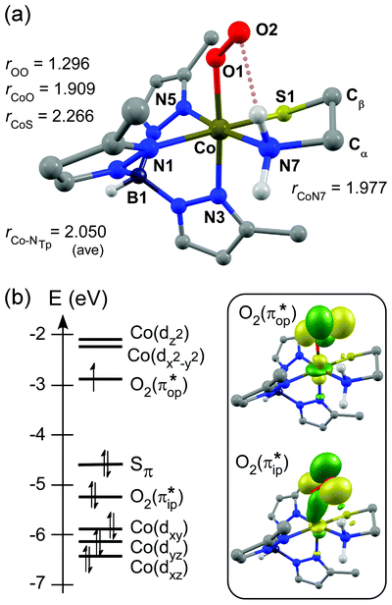

Fig. 10 (a) DFT geometry-optimized model of **4-O₂** with select bond distances indicated in angstroms (Å). (b) Energy-level diagram obtained from a spin-restricted DFT calculation of **4-O₂**. Isosurface plots of the superoxide-based π* MOs are shown in the inset.

The bonding description provided by DFT is consistent with the spectroscopic data. The computed *g*-values of 2.041, 2.006, and 1.989 replicate the quasi-axial nature of the experimental **g**-tensor, although the g_z-value is underestimated by DFT. The calculations predict a ^{59}Co A_z-value of 13 G, in line with the dramatic

decrease in ^{59}Co hyperfine splitting upon O_2 binding. Similarly, TD-DFT calculations yielded a computed absorption spectrum that nicely reproduces the energies and relative intensities of the major features of the experimental **4-O$_2$** spectrum (Fig. S2†). Based on analysis of the TD-DFT results, the band near 480 nm is assigned to overlapping $O_2^{\cdot-}(\pi_{op}^*) \rightarrow$ Co(3d) CT transitions, while the feature around 385 nm arises primarily from $S_\pi \rightarrow$ Co(3d) CT transitions.

DFT-computed mechanisms of sulfur dioxygenation by Co- and Fe-CDO models

Reaction mechanisms were examined with DFT methods to better understand the relative abilities of the Co- and Fe-CDO models to activate O_2 for *S*-dioxygenation. To this end, we have calculated the potential energies of intermediates and transition-states for the reaction of complex **4** with O_2 on both the $S = 1/2$ and 3/2 surfaces. The potential energy surfaces (PES's) are shown in Fig. 11 alongside the analogous PES previously-reported (by us) for Fe-containing **1** along the lowest-energy $S = 2$ surface.[49] Each set of calculations employed the PBE0 hybrid functional with 10% HF exchange, which provides reliable geometries and energies for species derived from the reaction of O_2 with transition-metal complexes.[90,91]

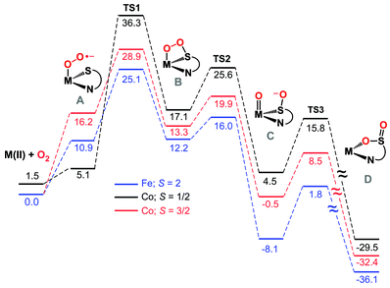

Fig. 11 Calculated potential energy profile for the *S*-dioxygenation reactions of Fe and Co CDO models **1**and **4**. Free energies (in kcal mol^{-1}) are relative to the starting five-coordinate M(ii) complexes and free triplet O_2.

The initial step involves coordination of O_2 to yield a six-coordinate M/O_2 species (**A^{M,S}**; where M is the metal ion and S is the spin state). Due to exchange interactions between the unpaired electrons of O_2 and the Co(ii) center, three spin-states are possible for the **A^{Co}** species: $S = 1/2$, 3/2, and 5/2. Attempts to optimize the **A$^{Co,\,S=5/2}$** structure failed, however, due to dissociation of the O_2 ligand; thus, the $S = 5/2$ surface was not considered further. In agreement with experiment, DFT predicts a low-spin ($S = 1/2$) ground state for **4-O$_2$**. The entropic contribution to O_2 binding is unfavorable for both the $S = 3/2$ and 1/2 states ($-T\Delta S = 14 \pm 2$ kcal mol^{-1} at 298 K; see Table S1†), as expected for a bimolecular reaction. Yet the enthalpic terms for the formation of **A$^{Co,\,S=3/2}$** and **A$^{Co,\,S=1/2}$** are quite different with computed values of +2.9 and −10.4 kcal mol^{-1}, respectively. Thus, as temperature decreases, the O_2 binding equilibrium shifts towards formation of the low-spin Co/O_2 adduct, consistent with our observation of **4-O$_2$** at $T < -20$ °C.

The role of ligand sterics in modulating the O_2 affinity of our Co-CDO models was also probed computationally. Analysis of the geometry-optimized model of **3-O$_2$** indicates that the phenyl rings of the Tp^{Ph2} ligand prevent the superoxo ligand from forming a strong hydrogen bond with the –NH_2 moiety of CysOEt. The loss of this stabilizing interaction diminishes the enthalpic driving force for O_2 binding to **3**, thus accounting for the fact that O_2 binding to **3** is not observed even at low temperatures (−80 °C).

The next step in the reaction mechanism requires formation of a cyclic M–O–O–S intermediate (**B^{M,S}**) *via* attack of the distal O-atom on the thiolate ligand. Previous DFT studies of CDO and related Fe-based models have identified this transformation as the rate-limiting step, and our results indicate that the same is true for the analogous Co-CDO complexes (Fig. 11). The barrier for O–S bond formation (**TS1**) on the $S = 1/2$ surface is significantly higher in energy (by 7.4 kcal mol^{-1}) than the same barrier on the $S = 3/2$ surface. Thus, further reaction of the low-spin [Co/O_2] adduct (**A$^{Co,\,S=1/2}$**) would likely require crossover to the $S = 3/2$ surface, which is kinetically unfavorable. The DFT results therefore account for the stability

of **4-O$_2$** at low temperature. It is also noteworthy that, regardless of spin state, substitution of Co for Fe raises the activation barrier for the rate-determining step by nearly 4 kcal mol^{-1}, in accordance with our experimental finding that Fe-CDO models are much more reactive towards O_2 than their Co counterparts.

The roles of spin-state and metal identity in promoting O–S bond formation become apparent when the electronic features of the various [M/O_2] adducts and **TS1** structures are compared. Mülliken populations indicate that the amount of spin-density localized on the S-atom in the [M/O_2] species varies greatly across the series, ranging from 0.27 ($\mathbf{A}^{\mathbf{Fe},\,S=2}$) to 0.19 ($\mathbf{A}^{\mathbf{Co},\,S=3/2}$) to 0.02 ($\mathbf{A}^{\mathbf{Co},\,S=1/2}$) spins. This parameter is critical because analysis of the **TS1**electronic structures reveals that formation of the cyclic intermediate requires overlap between partially-occupied S(3p) and $O_2(\pi_{ip}^*)$ orbitals carrying opposite spins. Thus, it is not surprising that the height of the **TS1** barrier is inversely correlated with the degree of S-radical character. The presence of paramagnetic Fe and Co centers in $\mathbf{A}^{\mathbf{Fe},\,S=2}$ and $\mathbf{A}^{\mathbf{Co},\,S=3/2}$, respectively, allows unpaired spin density to delocalize onto the thiolate ligand *via* metal–sulfur covalency. In contrast, the lack of unpaired-spin density on the S-atom of $\mathbf{A}^{\mathbf{Co},\,S=1/2}$, which accounts for the large **TS1** activation barrier on the $S = 1/2$ surface, is due the low-spin ($S = 0$) nature of its Co(iii) center (*vide supra*).

Each step in the reaction mechanism after formation of the cyclic M–O–O–S intermediate (**B**) is exergonic (Fig. 11). Heterolytic cleavage of the O–O bond yields either an iron(iv)-oxo ($\mathbf{C}^{\mathbf{Fe},S=2}$) or cobalt(iii)-oxyl ($\mathbf{C}^{\mathbf{Co},\,S=1/2}$ and $\mathbf{C}^{\mathbf{Co},\,S=3/2}$) species featuring a sulfenate ligand. This step is followed by insertion of the oxo/oxyl group into the metal–sulfur bond to generate the sulfinate product bound to the M(ii) center (**D**). The relative energies of intermediates **B** through **D**, as well as **TS2** and **TS3**, follow the same Fe ($S = 2$) < Co ($S = 3/2$) < Co ($S = 1/2$) pattern. Thus, the *S*-dioxygenation mechanism is most facile for the Fe-CDO model, consistent with our experimental observations.

Conclusions

In this manuscript, we have reported the synthesis of two mononuclear Co(ii) complexes (**3** and **4**) that serve as active-site mimics of cobalt-substituted CDO. Characterization with X-ray crystallography and/or ^{1}H NMR spectroscopy confirmed that **3** and **4** possess the intended 5C [Co(Tp^{R2})(CysOEt)] structure in which the CysOEt "substrate" coordinates in a *S,N*-bidentate manner. The facially-coordinating Tp^{R2} supporting ligands reproduce the 3His triad found in CDO active sites. Both complexes are brightly colored due to the presence of LF bands in the visible region and multiple S → Co(ii) peaks in the near-UV region. The X-band EPR spectra of **3**and **4** display an abundance of features across a wide field range. These resonances arise from intra-Kramers transitions within both doublets ($m_s = \pm 3/2$ and $\pm 1/2$) of the $S = 3/2$ ground state. Simulation of the experimental data provided spin-Hamiltonian parameters for **3** and **4** that are consistent with distorted 5C geometries.

Complex **3** represents the cobalt analog of the previously-reported Fe-based CDO model **1**, which was shown to react with O_2 to yield the sulfinic acid of CysOEt.[46] In contrast, **3** is unreactive towards O_2 over the span of multiple days, thereby replicating the inactivity of Co-substituted CDO. The O_2 affinity of the Co(ii) center, however, is somewhat dependent on the steric profile and donor strength of the Tp^{R2} supporting ligand. Complex **4**, which features the less bulky and more electron-donating Tp^{Me2} ligand, reversibly binds O_2 at reduced temperatures to yield a low-spin ($S = 1/2$) Co/O_2 adduct (**4-O$_2$**), as verified by EPR and rRaman spectroscopies. Similar Co/O_2 intermediates have been implicated in the mechanisms of biological and synthetic oxidation catalysts. The relative stability of **4-O$_2$** is due to two factors: (i) the nearly complete electron transfer from Co(ii) to O_2, which generates a kinetically-inert low-spin Co(iii) center bound to a superoxide anion, and (ii) the hydrogen bond between superoxide and the –NH_2 group of CysOEt.

The putative O_2 activation mechanisms of the Co- and Fe-CDO models were further probed with DFT computations. These calculations revealed that the low-spin Co/O_2 species (*i.e.*, **4-O$_2$**) represents a mechanistic "dead-end", as the barrier leading to formation of the S–O bond in the next step is very high

(>30 kcal mol^{-1}). In contrast, the less stable high-spin Co/O_2 ($S = 3/2$) and Fe/O_2 ($S = 2$) adducts delocalize spin density onto CysOEt ligand *via* metal–thiolate covalency, resulting in a significant degree of S-radical character that lowers the transition-state barrier to S–O bond formation. In many respects, the **4-O_2** intermediate resembles the Co/O_2species observed in studies of cobalt-substituted homoprotocatechuate dioxygenase (Co-HPCD) that employed the electron-poor substrate, 4-nitrocatechol (4-NC). Exposure of Co-HPCD/4-NC to O_2 generates a $S = 1/2$ cobalt(iii)-superoxo adduct with EPR features similar to those reported for **4-O_2**.[57] While the Co-HPCD/4-NC/O_2 species decays to give to the ring-cleaved product, the rate is seven orders of magnitude slower than the analogous reaction with Fe-HPCD/4-NC. The lower activity of Co-HPCD relative to Fe-HPCP has been attributed to a lack of semiquinone (SQ) radical character in the Co-HPCD/4-NC/O_2 species[57,58] – a hypothesis that parallels our explanation for the contrasting reactivities of Co- and Fe-CDO models towards O_2. Interestingly, under conditions of O_2 saturation, the activity of Co-HPCD with the native homoprotocatechuate substrate is actually greater than the activity of Fe-HPCD. Although intermediates have not been observed in this case, DFT calculations suggested that use of the more electron-rich substrate yields a high-spin $O_2^{\cdot-}$/Co(ii)/SQ intermediate with $S = 3/2$, which encourages formation of the Co–O–O–C intermediate.[92]

In summary, the results presented here suggest that HPCD and CDO operate *via* similar mechanisms that each require full (or partial) oxidation of the bound substrate upon O_2 binding, thereby permitting facile reaction with the superoxo ligand. The inactivity of Co-CDO is attributed to the lack of unpaired spin-density present on the thiolate donor of the low-spin Co/O_2 adduct. Moreover, our findings support the conclusion that Co-substituted forms of MNIDs only exhibit activity comparable to the native Fe enzymes in cases when high-spin Co/O_2 intermediates are energetically accessible.

Experimental

Materials

All reagents and solvents were purchased from commercial sources and used as received, unless otherwise noted. Dichloromethane (CH_2Cl_2) and acetonitrile (MeCN) were purified and dried using a Vacuum Atmospheres solvent purification system and stored under N_2. The synthesis and handling of air-sensitive materials were performed under inert atmosphere using a Vacuum Atmospheres Omni-Lab glovebox. The ligand K(Tp^{Ph2}) was prepared according to a literature procedure.[93]

Physical methods

UV-vis absorption spectra were collected with an Agilent 8453 diode array spectrometer attached to a cryostat manufactured by Unisoku Scientific Instruments (Osaka, Japan) for measurements at reduced temperatures. Infrared (IR) spectra were collected with a Nicolet Magna-IR 560 spectrometer. X-band EPR spectra were measured using a Bruker EMXplus instrument equipped with an ER4416DM cavity, an Oxford Instruments ESR900 helium flow cryostat, and Oxford Instruments ITC503 temperature controller. Simulations of the experimental EPR spectra were performed using the program EasySpin (version 5).[94]^{1}H NMR samples were prepared in deuterated solvents and spectra were recorded on a Varian 400 MHz spectrometer. Cyclic voltammograms were measured in the glovebox with an epsilon EC potentiostat (iBAS) at a scan rate of 200 mV s^{-1} with 0.1 M [NBu_4]PF_6 electrolyte. The three-electrode cell consisted of a Ag/AgCl reference electrode, a platinum auxiliary electrode, and a glassy carbon working electrode. Under these conditions, the ferrocene/ferrocenium ($Fc^{+/0}$) couple has an $E_{1/2}$ value of +0.51 V in CH_2Cl_2. Elemental analyses were performed at Midwest Microlab, LLC in Indianapolis, IN.

Synthesis of [Co(Tp^{Me2})(OAc)] (5)

Using a modified literature procedure,[95] $Co(OAc)_2{\cdot}4H_2O$ (0.747 g, 3.0 mmol) was dissolved in MeOH (20 mL) and a solution of K(^{Me2}Tp) (0.673 g, 2.0 mmol) in THF (20 mL) was added dropwise. After the addition was complete, the solution was filtered and the solvent removed under vacuum. The product was then

extracted with CH_2Cl_2 and dried under vacuum, followed by another extraction with MeCN. Removal of solvent *en vacuo* provided a purple solid that was taken up in CH_2Cl_2, filtered, and layered with pentane. Crystalline purple solid formed after one day. Yield = 400 mg (48%). X-ray quality crystals were formed by layering a more dilute CH_2Cl_2solution of **5** with pentane. UV-vis [λ_{max}, nm (ε, M^{-1} cm^{-1}) in CH_2Cl_2]: 305 (700), 573 (90). FTIR (cm^{-1}, solution): 1543 (CO_2, antisym). ^{1}H NMR (400 MHz, $CDCl_3$): δ = 61.5 (3H, 4-pz), 54.8 (1H, B*H*), 35.1 (9H, 5Me-pz), −40.8 (9H, 3Me-pz) ppm.

Synthesis of [Co(Tp^{Ph2})(CysOEt)] (3)

l-Cysteine ethyl ester hydrochloride (56 mg, 0.30 mmol) and triethylamine (92 µL, 0.66 mmol) were dissolved in CH_2Cl_2 (10 mL) and stirred until all of the solid dissolved. Dropwise addition of [Co(Tp^{Ph2})(OAc)(Hpz^{Ph2})][66] (202 mg, 0.20 mmol) in CH_2Cl_2 generated a brown solution that was stirred for 3 hours. The volume of the solvent was reduced under vacuum, filtered, and then layered with MeCN. Dark-brown crystals suitable for X-ray analysis formed after one day. Yield = 138 mg (79%). Anal. calcd for $C_{50}H_{44}BCoN_7O_2S$ (M_w = 876.74 g mol^{-1}): C, 68.50; H, 5.06; N, 11.18. Found: C, 69.33; H, 5.15; N, 11.23. UV-vis [λ_{max}, nm (ε, M^{-1} cm^{-1}) in CH_2Cl_2]: 349 (2460), 378 (sh), 438 (380), 546 (120). FTIR (cm^{-1}, solution): 3357 (N–H), 1729 (C=O). ^{1}H NMR (400 MHz, $CDCl_3$): δ = 77.0 (1H, B*H*), 46.7 (4-pz, 3H), 27.7 (6H), 17.7 (6H), 14.7 (3H), 4.4 (9H), −5.2 (3H, OCH_2CH_3), −5.4 (1H), −6.8 (1H), −39.9 (6H), −48.6 (1H) ppm.

Synthesis of [Co(Tp^{Me2})(CysOEt)] (4)

A solution of l-cysteine ethyl ester hydrochloride (56 mg, 0.30 mmol) and triethylamine (92 µL, 0.66 mmol) in CH_2Cl_2 (10 mL) was stirred until the former compound had fully dissolved. Dropwise addition of **5** (84 mg, 0.20 mmol) in CH_2Cl_2 provided a dark purple solution that was stirred for 3 hours. Afterwards, the solution was filtered and the solvent removed under vacuum. The resulting solid was extracted with toluene and dried under vacuum to yield the crude product. Subsequent extraction with MeCN, followed by removal of solvent *en vacuo*, yielded the pure complex as a purple powder. Yield = 72 mg (71%). Anal. calcd for $C_{20}H_{32}BCoN_7O_2S$ (M_w = 504.32 g mol^{-1}): C, 47.63; H, 6.40; N, 19.44. Found: C, 47.39; H, 6.16; N, 18.68. UV-vis [λ_{max}, nm (ε, M^{-1} cm^{-1}) in CH_2Cl_2]: 328 (2310), 395 (460), 543 (125). FTIR (cm^{-1}, solution): 3345 (N–H), 1729 (C=O). ^{1}H NMR (400 MHz, $CDCl_3$): δ = 62.5 (1H, B*H*), 51.7 (3H, 4-pz), 32.0 (9H, 5Me-pz), 1.3 (2H, OCH_2CH_3) −4.1 (3H, OCH_2CH_3), −5.3 (1H), −6.6 (1H), −48.1 (1H), −51.7 (9H, 3Me-pz) ppm.

X-ray crystallography

X-ray crystal structures were obtained at 100 K with an Oxford Diffraction SuperNova kappa-diffractometer (Rigaku Corp.) equipped with dual Cu/Mo X-ray sources, X-ray mirror optics, an Atlas CCD detector, and a low-temperature Cryojet device. The data were processed with the CrysAlis Pro program package, followed by numerical absorption correction based on Gaussian integration over a multifaceted crystal model. The empirical absorption correction, using spherical harmonics, was implemented in the SCALE3 ABSPACK scaling algorithm. Structures were solved using the SHELXS program and refined with the SHELXL program[96] as part of the Olex2 crystallographic package.[97] X-ray diffraction parameters are summarized below; CCDC 1545173 and 1545174 contain the supplementary crystallographic data (CIF files) for complexes **3** and **5**, respectively, reported in this paper.

Crystallographic data for complex **3**: $C_{50}H_{44}BCoN_7O_2S$, M_r = 876.72 g mol^{-1}, monoclinic, space group $P2_1$, a = 15.77282(13), b = 16.76061(12), c = 16.80269(14) Å, α = 90, β = 91.5914(7), γ = 90°, V = 4440.28(6) $Å^3$, Z = 4, ρ = 1.311 g cm^{-3}, reflections collected 40 090, independent reflections 16 708 (R_{int} = 0.0435), 1124 parameters, R_1 = 0.0489 and wR_2 = 0.1354 for $I \geq 2\sigma(I)$.

Crystallographic data for complex **5**: $C_{17}H_{25}BCoN_6O_2$, M_r = 415.17 g mol^{-1}, monoclinic, space group $P2_1/c$, a = 13.7807(3), b = 7.71018(14), c = 18.8008(3) Å, α = 90, β = 103.778(2), γ = 90°, V = 1940.14(6) $Å^3$, Z = 4, ρ = 1.421 g cm^{-3}, reflections collected 22 252, independent reflections 4939 (R_{int} = 0.0503), 251 parameters, R_1 = 0.0461 and wR_2 = 0.1177 for $I \geq 2\sigma(I)$.

Resonance Raman (rRaman) experiments

To prepare rRaman samples of **4-O_2**, solutions of **4** in CD_2Cl_2 (conc. = 6.9 mM) were added to NMR tubes and attached to a Schlenk line. The tubes were cooled to −78 °C and several vacuum/argon cycles were performed, followed by exposure to gaseous dioxygen ($^{16}O_2$ or $^{18}O_2$). After mixing with a Vortex stirrer, the **4-O_2** samples were frozen in liquid N_2 and detached from the Schlenk line. The rRaman data were measured using 501.7 nm excitation from a Coherent I-305 Ar^+ laser (~10 mW of power at the sample). The light scattered from the frozen samples (77 K) was collected using a 135° backscattering arrangement and dispersed by an Acton Research triple monochromator featuring a 1200 groves per mm grating. The scattered light was detected with a Princeton Instruments Spec X 100BR deep depletion, back-thinned CCD camera.

Density functional theory (DFT) computations

DFT calculations were performed with the ORCA 3.0 software package developed by Dr F. Neese (MPI for Chemical Energy Conversion).[98] All calculations employed the spin-unrestricted formalism, unless otherwise noted. Geometries were optimized with the Perdew–Burke–Ernzerhof (PBE0) hybrid functional[99] with 10% Hartree–Fock exchange. Calculations utilized Ahlrichs' valence triple-ζ basis set (TZV) and polarization functions on main-group and transition-metal elements (default-basis 3 in ORCA).[100–102] The computational costs were reduced through the resolution of identity and chain of sphere (RIJCOSX) approximation[103] in tandem with the TZV/J auxiliary basis set.[104] The unrestrained optimizations used modified versions of the X-ray crystal structures of **1** and **3** as starting points. In most cases, the Tp^{R2}supporting ligand was truncated to hydrotris(3-methylpyrazolyl)borate (*i.e.*, $Tp^{Me,H}$); however, studies of O_2 binding to complex **3** employed a $Tp^{Ph,H}$ ligand instead. The models omit the ethyl ester moieties of the CysOEt ligand, as previous calculations indicated that this group has little impact on molecular geometries, electronic structures, or relative energies. All optimized structures correspond to local energy minima with only real vibrational frequencies. The transition states were located by performing a relaxed surface scan along the bond being formed (or broken); the existence of the transition state was confirmed by the presence of one imaginary frequency corresponding to the bond forming (or breaking) mode. Frequency calculations provided zero-point energies, thermal corrections, and entropy terms (vibrational, rotational, and translational). Cartesian coordinates for all energy-minimized and transition-state structures are provided in the ESI (Tables S2–25†).

Time-dependent DFT (TD-DFT) calculations employed the cam-B3LYP range-separated hybrid functional,[80] which has been shown to provide good agreement between experimental and TD-DFT computed absorption spectra for CDO.[105] Absorption energies and intensities were computed for 40 excited states with the Tamm-Dancoff approximation.[106,107] EPR *g*-values were calculated by solving the coupled-perturbed self-consistent field (CP-SCF) equations.[108–111] Isosurface plots of molecular orbitals were prepared using the ChemCraft program.

Acknowledgements

This research received financial support from the U.S. National Science Foundation (CHE-1056845), including funding to upgrade the X-band EPR instrument at Marquette University (CHE-1532168). We are grateful to Dr Thomas Brunold (University of Wisconsin – Madison) for access to rRaman instrumentation. Anne Fischer was the beneficiary of a research fellowship provided by the Denis J. O'Brien Fund of Marquette University.

References

1. C. A. Joseph and M. J. Maroney , *Chem. Commun.*, 2007, 3338 -3349 .
2. K. Yamaguchi and Y. Hosokawa , *Methods Enzymol.*, 1987, **143** , 395 -403 .

3. M. H. Stipanuk , C. R. Simmons , P. Andrew Karplus and J. E. Dominy Jr. , *Amino Acids*, 2011,**41** , 91 -102 .
4. X. W. Li , M. Guo , J. Fan , W. Y. Tang , D. Q. Wang , H. H. Ge , H. Rong , M. K. Teng , L. W. Niu ,Q. Liu and Q. Hao , *Protein Sci.*, 2006, **15** , 761 -773 .
5. Y. Zhang , K. L. Colabroy , T. P. Begley and S. E. Ealick , *Biochemistry*, 2005, **44** , 7632 -7643
6. I. Efimov , J. Basran , S. J. Thackray , S. Handa , C. G. Mowat and E. L. Raven , *Biochemistry*, 2011, **50** , 2717 -2724 .
7. J. Geng and A. Liu , *Arch. Biochem. Biophys.*, 2014, **544** , 18 -26 .
8. L.-F. Wu , S. Meng and G.-L. Tang , *Biochim. Biophys. Acta, Proteins Proteomics*, 2016, **1864** , 453 -470 .
9. R. V. K. Cochrane and J. C. Vederas , *Acc. Chem. Res.*, 2014, **47** , 3148 -3161 .
10. K. H. Baker and D. S. Herson , *Bioremediation* , K. H. Baker and D. S. Herson, McGraw-Hill, Inc., New York, 1994, 9–60 .
11. A. Singh and O. P. Ward , *Biodegradation and Bioremediation* , A. Singh and O. P. Ward, Springer, Heidelberg, 2004, 1–18 .
12. R. E. Parales and J. D. Haddock , *Curr. Opin. Biotechnol.*, 2004, **15** , 374 -379 .
13. L. P. Wackett and C. D. Hershberger , *Biocatalysis and Biodegradation: Microbial Transformation of Organic Compounds* , ASM Press, Washington, D.C., 2001, .
14. D. T. Gibson and R. E. Parales , *Curr. Opin. Biotechnol.*, 2000, **11** , 236 -243 .
15. R. Parales and S. M. Resnick , *Biodegradation and Bioremediation* , A. Singh and O. P. Ward, Springer, Heidelberg, 2004, 175–196 .
16. S. Kal and L. Que , *J. Biol. Inorg. Chem.*, 2017, **22** , 339 -365 .
17. K. D. Koehntop , J. P. Emerson and L. Que , *J. Biol. Inorg. Chem.*, 2005, **10** , 87 -93 .
18. E. L. Hegg and L. Que Jr. , *Eur. J. Biochem.*, 1997, **250** , 625 -629 .
19. G. D. Straganz and B. Nidetzky , *ChemBioChem*, 2006, **7** , 1536 -1548 .
20. A. R. Diebold , M. L. Neidig , G. R. Moran , G. D. Straganz and E. I. Solomon , *Biochemistry*, 2010, **49** , 6945 -6952 .
21. D. Buongiorno and G. D. Straganz , *Coord. Chem. Rev.*, 2013, **257** , 541 -563 .
22. J. G. McCoy , L. J. Bailey , E. Bitto , C. A. Bingman , D. J. Aceti , B. G. Fox and G. N. Phillips Jr. , *Proc. Natl. Acad. Sci. U. S. A.*, 2006, **103** , 3084 -3089 .
23. C. R. Simmons , Q. Liu , Q. Q. Huang , Q. Hao , T. P. Begley , P. A. Karplus and M. H. Stipanuk , *J. Biol. Chem.*, 2006, **281** , 18723 -18733 .
24. A. Slivka and G. Cohen , *Brain Res.*, 1993, **608** , 33 -37 .
25. A. R. Pean , R. B. Parsons , R. H. Waring , A. C. Williams and D. B. Ramsden , *J. Neurosci.*, 1995, **129** , 107 -108 .
26. M. T. Heafield , S. Fearn , G. B. Steventon , R. H. Waring , A. C. Williams and S. G. Sturman , *Neurosci. Lett.*, 1990, **110** , 216 -220 .
27. T. L. Perry , M. G. Norman , V. W. Yong , S. Whiting , J. U. Crichton , S. Hansen and S. J. Kish , *Ann. Neurol.*, 1985, **18** , 482 -489 .
28. M. Brait , S. Ling , J. K. Nagpal , X. Chang , H. L. Park , J. Lee , J. Okamura , K. Yamashita , D. Sidransky and M. S. Kim , *PLoS One*, 2012, **7** , e44951 .
29. A. T. Fiedler and A. A. Fischer , *JBIC, J. Biol. Inorg. Chem.*, 2017, **22** , 407 -424 .
30. S. C. Chai , J. R. Bruyere and M. J. Maroney , *J. Biol. Chem.*, 2006, **281** , 15774 -15779 .
31. S. Ye , X. A. Wu , L. Wei , D. Tang , P. Sun , M. Bartlam and Z. Rao , *J. Biol. Chem.*, 2007, **282** , 3391 -3402 .
32. C. M. Driggers , K. M. Kean , L. L. Hirschberger , R. B. Cooley , M. H. Stipanuk and P. A. Karplus, *J. Mol. Biol.*, 2016, **428** , 3999 -4012 .
33. C. M. Driggers , R. B. Cooley , B. Sankaran , L. L. Hirschberger , M. H. Stipanuk and P. A. Karplus , *J. Mol. Biol.*, 2013, **425** , 3121 -3136 .

34. B. S. Pierce , J. D. Gardner , L. J. Bailey , T. C. Brunold and B. G. Fox , *Biochemistry*, 2007, **46** , 8569 -8578 .
35. J. A. Crawford , W. Li and B. S. Pierce , *Biochemistry*, 2011, **50** , 10241 -10253 .
36. D. Kumar , W. Thiel and S. P. de Visser , *J. Am. Chem. Soc.*, 2011, **133** , 3869 -3882 .
37. S. Aluri and S. P. De Visser , *J. Am. Chem. Soc.*, 2007, **129** , 14846 -14847 .
38. E. J. Blaesi , J. D. Gardner , B. G. Fox and T. C. Brunold , *Biochemistry*, 2013, **52** , 6040 -6051 .
39. E. J. Blaesi , B. G. Fox and T. C. Brunold , *Biochemistry*, 2014, **53** , 5759 -5770 .
40. E. P. Tchesnokov , A. S. Faponle , C. G. Davies , M. G. Quesne , R. Turner , M. Fellner , R. J. Souness , S. M. Wilbanks , S. P. de Visser and G. N. L. Jameson , *Chem. Commun.*, 2016, **52** , 8814 -8817 .
41. Y. Jiang , L. R. Widger , G. D. Kasper , M. A. Siegler and D. P. Goldberg , *J. Am. Chem. Soc.*, 2010, **132** , 12214 -12215 .
42. A. C. McQuilken , Y. Jiang , M. A. Siegler and D. P. Goldberg , *J. Am. Chem. Soc.*, 2012, **134** , 8758 -8761 .
43. A. C. McQuilken , Y. Ha , K. D. Sutherlin , M. A. Siegler , K. O. Hodgson , B. Hedman , E. I. Solomon , G. N. L. Jameson and D. P. Goldberg , *J. Am. Chem. Soc.*, 2013, **135** , 14024 -14027 .
44. A. C. McQuilken and D. P. Goldberg , *Dalton Trans.*, 2012, **41** , 10883 -10899 .
45. Y. M. Badiei , M. A. Siegler and D. P. Goldberg , *J. Am. Chem. Soc.*, 2011, **133** , 1274 -1277 .
46. M. Sallmann , I. Siewert , L. Fohlmeister , C. Limberg and C. Knispel , *Angew. Chem., Int. Ed.*, 2012, **51** , 2234 -2237 .
47. M. Sallmann , B. Braun and C. Limberg , *Chem. Commun.*, 2015, **51** , 6785 -6787 .
48. M. Sallmann , S. Kumar , P. Chernev , J. Nehrkorn , A. Schnegg , D. Kumar , H. Dau , C. Limberg and S. P. de Visser , *Chem. – Eur. J.*, 2015, **21** , 7470 -7479 .
49. A. A. Fischer , N. Stracey , S. V. Lindeman , T. C. Brunold and A. T. Fiedler , *Inorg. Chem.*, 2016,**55** , 11839 -11853 .
50. L. J. Ming , L. Que Jr. , A. Kriauciunas , C. A. Frolik and V. J. Chen , *Biochemistry*, 1991, **30** , 11653 -11659 .
51. E. D. Coulter , N. Moon , C. J. Batie , W. R. Dunham and D. P. Ballou , *Biochemistry*, 1999, **38** , 11062 -11072 .
52. B. Bleijlevens , T. Shivarattan , B. Sedgwick , S. E. J. Rigby and S. J. Matthews , *J. Inorg. Biochem.*, 2007, **101** , 1043 -1048 .
53. E. L. Hegg , A. K. Whiting , R. E. Saari , J. McCracken , R. P. Hausinger and L. Que Jr. , *Biochemistry*, 1999, **38** , 16714 -16726 .
54. J. P. Emerson , E. G. Kovaleva , E. R. Farquhar , J. D. Lipscomb and L. Que , *Proc. Natl. Acad. Sci. U. S. A.*, 2008, **105** , 7347 -7352 .
55. A. J. Fielding , E. G. Kovaleva , E. R. Farquhar , J. D. Lipscomb and L. Que Jr. , *J. Biol. Inorg. Chem.*, 2011, **16** , 341 -355 .
56. W. A. Gunderson , A. I. Zatsman , J. P. Emerson , E. R. Farquhar , L. Que , J. D. Lipscomb andM. P. Hendrich , *J. Am. Chem. Soc.*, 2008, **130** , 14465 -14467 .
57. A. J. Fielding , J. D. Lipscomb and L. Que , *J. Am. Chem. Soc.*, 2012, **134** , 796 -799 .
58. A. J. Fielding , J. D. Lipscomb and L. Que Jr. , *J. Biol. Inorg. Chem.*, 2014, **19** , 491 -504 .
59. C. W. Anson , S. Ghosh , S. Hammes-Schiffer and S. S. Stahl , *J. Am. Chem. Soc.*, 2016, **138** , 4186 -4193 .
60. A. R. Corcos , O. Villanueva , R. C. Walroth , S. K. Sharma , J. Bacsa , K. M. Lancaster , C. E. MacBeth and J. F. Berry , *J. Am. Chem. Soc.*, 2016, **138** , 1796 -1799 .
61. K. Mittra , B. Mondal , A. Mahammed , Z. Gross and A. Dey , *Chem. Commun.*, 2017, **53** , 877 -880 .
62. K. Mase , S. Aoi , K. Ohkubo and S. Fukuzumi , *J. Porphyrins Phthalocyanines*, 2016, **20** , 935 -949 .
63. D. K. Dogutan , S. A. Stoian , R. McGuire , M. Schwalbe , T. S. Teets and D. G. Nocera , *J. Am. Chem. Soc.*, 2011, **133** , 131 -140 .

64. C.-C. Wang , H.-C. Chang , Y.-C. Lai , H. Fang , C.-C. Li , H.-K. Hsu , Z.-Y. Li , T.-S. Lin , T.-S. Kuo , F. Neese , S. Ye , Y.-W. Chiang , M.-L. Tsai , W.-F. Liaw and W.-Z. Lee , *J. Am. Chem. Soc.*, 2016, **138** , 14186 -14189 .
65. I. G. Dance , M. Gerloch , J. Lewis , F. S. Stephens and F. Lions , *Nature*, 1966, **210** , 298.
66. D. J. Harding , P. Harding , R. Daengngern , S. Yimklan and H. Adams , *Dalton Trans.*, 2009, 1314 - 1320 .
67. A five-coordinate complex with ideal square-pyramidal geometry would have a τ-value of 0.0, while those with ideal trigonal bipyramidal geometry would have a value of 1.0
68. A. W. Addison , T. N. Rao , J. Reedijk , J. Vanrijn and G. C. Verschoor , *J. Chem. Soc., Dalton Trans.*, 1984, 1349 -1356 .
69. F. E. Jacobsen , R. M. Breece , W. K. Myers , D. L. Tierney and S. M. Cohen , *Inorg. Chem.*, 2006, **45** , 7306 -7315 .
70. A. R. Marts , J. C. Kaine , R. R. Baum , V. L. Clayton , J. R. Bennett , L. J. Cordonnier , R. McCarrick , A. Hasheminasab , L. A. Crandall , C. J. Ziegler and D. L. Tierney , *Inorg. Chem.*, 2017, **56** , 618 -626 .
71. H. Park , M. M. Bittner , J. S. Baus , S. V. Lindeman and A. T. Fiedler , *Inorg. Chem.*, 2012, **51** , 10279 - 10289 .
72. H. Park , J. S. Baus , S. V. Lindeman and A. T. Fiedler , *Inorg. Chem.*, 2011, **50** , 11978 -11989.
73. M. P. Mehn , K. Fujisawa , E. L. Hegg and L. Que , *J. Am. Chem. Soc.*, 2003, **125** , 7828 -7842.
74. M. Ciampolini , N. Nardi and G. P. Speroni , *Coord. Chem. Rev.*, 1966, **1** , 222 -233 .
75. A. B. P. Lever *Inorganic Electronic Spectroscopy* , Elsevier, Amsterdam, 1968, .
76. J. A. Larrabee , C. M. Alessi , E. T. Asiedu , J. O. Cook , K. R. Hoerning , L. J. Klingler , G. S. Okin , S. G. Santee and T. L. Volkert , *J. Am. Chem. Soc.*, 1997, **119** , 4182 -4196 .
77. D. C. Fox , A. T. Fiedler , H. L. Halfen , T. C. Brunold and J. A. Halfen , *J. Am. Chem. Soc.*, 2004, **126** , 7627 -7638 .
78. L. M. Brines , G. Villar-Acevedo , T. Kitagawa , R. D. Swartz , P. Lugo-Mas , W. Kaminsky , J. B. Benedict and J. A. Kovacs , *Inorg. Chim. Acta*, 2008, **361** , 1070 -1078 .
79. J. S. Thompson , T. Sorrell , T. J. Marks and J. A. Ibers , *J. Am. Chem. Soc.*, 1979, **101** , 4193 -4201 .
80. T. Yanai , D. P. Tew and N. C. Handy , *Chem. Phys. Lett.*, 2004, **393** , 51 -57 .
81. A. R. Marts , S. M. Greer , D. R. Whitehead , T. M. Woodruff , R. M. Breece , S. W. Shim , S. N. Oseback , E. T. Papish , F. E. Jacobsen , S. M. Cohen and D. L. Tierney , *Appl. Magn. Reson.*, 2011, **40** , 501 -511 .
82. T. D. Smith and J. R. Pilbrow , *Coord. Chem. Rev.*, 1981, **39** , 295 -383 .
83. M. Baumgarten , C. J. Winscom and W. Lubitz , *Appl. Magn. Reson.*, 2001, **20** , 35 -70 .
84. B. Ramdhanie , J. Telser , A. Caneschi , L. N. Zakharov , A. L. Rheingold and D. P. Goldberg , *J. Am. Chem. Soc.*, 2004, **126** , 2515 -2525 .
85. F. Oddon , Y. Chiba , J. Nakazawa , T. Ohta , T. Ogura and S. Hikichi , *Angew. Chem., Int. Ed.*, 2015, **54** , 7336 -7339 .
86. K. Bajdor , J. R. Kincaid and K. Nakamoto , *J. Am. Chem. Soc.*, 1984, **106** , 7741 -7747 .
87. C.-W. Chiang , S. T. Kleespies , H. D. Stout , K. K. Meier , P.-Y. Li , E. L. Bominaar , L. Que , E. Munck and W.-Z. Lee , *J. Am. Chem. Soc.*, 2014, **136** , 10846 -10849 .
88. M. T. Kieber-Emmons , J. Annaraj , M. S. Seo , K. M. VanHeuvelen , T. Tosha , T. Kitagawa , T. C. Brunold , W. Nam and C. G. Riordan , *J. Am. Chem. Soc.*, 2006, **128** , 14230 -14231 .
89. K. Ray , F. F. Pfaff , B. Wang and W. Nam , *J. Am. Chem. Soc.*, 2014, **136** , 13942 -13958 .
90. G. Schenk , M. Y. M. Pau and E. I. Solomon , *J. Am. Chem. Soc.*, 2004, **126** , 505 -515.
91. M. M. Bittner , S. V. Lindeman , C. V. Popescu and A. T. Fiedler , *Inorg. Chem.*, 2014, **53** , 4047 -4061 .
92. L. Cao , G. Dong and W. Lai , *J. Phys. Chem. B*, 2015, **119** , 4608 -4616 .
93. N. Kitajima , K. Fujisawa , C. Fujimoto , Y. Morooka , S. Hashimoto , T. Kitagawa , K. Toriumi ,K. Tatsumi and A. Nakamura , *J. Am. Chem. Soc.*, 1992, **114** , 1277 -1291 .
94. S. Stoll and A. Schweiger , *J. Magn. Reson.*, 2006, **178** , 42 -55 .

95. S. Hikichi , Y. Sasakura , M. Yoshizawa , Y. Ohzu , Y. Moro-oka and M. Akita , *Bull. Chem. Soc. Jpn.*, 2002, **75** , 1255 -1262 .
96. G. M. Sheldrick *Acta Crystallogr., Sect. A: Fundam. Crystallogr.*, 2008, **64** , 112 -122 .
97. O. V. Dolomanov , L. J. Bourhis , R. J. Gildea , J. A. K. Howard and H. Puschmann , *J. Appl. Crystallogr.*, 2009, **42** , 339 -341 .
98. F. Neese *WIREs Comput. Mol. Sci.*, 2012, **2** , 73 -78 .
99. J. P. Perdew , K. Burke and M. Ernzerhof , *Phys. Rev. Lett.*, 1996, **77** , 3865 -3868 .
100. A. Schafer , C. Huber and R. Ahlrichs , *J. Chem. Phys.*, 1994, **100** , 5829 -5835 .
101. A. Schafer , H. Horn and R. Ahlrichs , *J. Chem. Phys.*, 1992, **97** , 2571 -2577 .
102. F. Weigend and R. Ahlrichs , *Phys. Chem. Chem. Phys.*, 2005, **7** , 3297 -3305 .
103. F. Neese , F. Wennmohs , A. Hansen and U. Becker , *Chem. Phys.*, 2009, **356** , 98 -109
104. K. Eichkorn , O. Treutler , H. Oehm , M. Haeser and R. Ahlrichs , *Chem. Phys. Lett.*, 1995, **240** , 283 -290
105. E. J. Blaesi , B. G. Fox and T. C. Brunold , *Biochemistry*, 2015, **54** , 2874 -2884
106. S. Hirata and M. Head-Gordon , *Chem. Phys. Lett.*, 1999, **314** , 291 -299
107. S. Hirata and M. Head-Gordon , *Chem. Phys. Lett.*, 1999, **302** , 375 -382
108. F. Neese *Curr. Opin. Chem. Biol.*, 2003, **7** , 125 -135
109. F. Neese *J. Chem. Phys.*, 2001, **115** , 11080 -11096
110. S. Sinnecker , F. Neese , L. Noodleman and W. Lubitz , *J. Am. Chem. Soc.*, 2004, **126** , 2613 -2622
111. F. Neese *J. Chem. Phys.*, 2003, **118** , 3939 -3948

Footnote

1. † Electronic supplementary information (ESI) available. CCDC 1545173 and 1545174. For ESI and crystallographic data in CIF or other electronic format see DOI: 10.1039/c7dt01600j